SUPPLEMENTARY INFORMATION

Supplementary Information

1. Supplementary Text

1A. Formation heights of Hα and Ca IRT lines in the chromosphere

All three targets in this study **have small** $v \sin i$ values (Table S1). Consequently, the unpolarized, disk-integrated profiles we observed closely approximate the mean profiles derived from all disk pixels. We observed that all Hα profiles display a well-known two-peak structure, consistent with predictions from Non-local Thermodynamic Equilibrium (NLTE) atmospheric models [1, 2].

For solar active regions, longitudinal magnetic fields detected through Hα line wings originate from the bottom of the chromosphere, whereas the line core emanates from the mid-to-upper chromosphere, similar to the core of Ca IRT [3]. Figure S2 shows an example of the two-peak structure of Hα in Stokes I and corresponding V profiles. We use standard indicators for the structure: the line-center depression (Hα3), the violet and red emission peaks (Hα2v and Hα2r), and the flux minima (Hα1v and Hα1r). The wings of the profile are between Hα1x and Hα2x (x can be v or r).

To evaluate the strength of the circular polarization signal, we calculated the average absolute ratio between V and I profiles ($|V/I|$) for both the wings and core of the line profile. We found that the average $|V/I|$ of the wings is at least twice that of the core, suggesting that the Stokes V signal in Hα is predominantly detected within the wings of the Stokes I profiles. Hence, the detected magnetic field in the Hα profiles should be attributed to a lower height in the chromosphere.

According to solar observations [3], the core of Ca IRT is formed in the middle chromosphere and its polarization profiles can be used to detect the fields there.

1B. Variation of the measured longitudinal magnetic field with height

The variation patterns of the longitudinal magnetic field $\langle B_l \rangle$ measurements shown in Figure 2 are predominantly influenced by the large-scale magnetic field structures[4]. As shown in Figure S3, the measurements of YZ CMi in the selected epoch generally form one repeating pattern in the phase-folded diagram, indicating that the large-scale magnetic fields are generally stable in one epoch by neglecting the differential rotation of the stars. For AD Leo EV Lac, their patterns are less clear than YZ CMi, but they can be fitted by a double sine function as shown in Figure 2. The large-scale magnetic fields in the photosphere of all three targets generally exhibited a dipole structure[4–6]. However, the magnetic axis for these stars was not precisely aligned with the rotational axis, particularly for YZ CMi and EV Lac. Additionally, the inclination angle between the rotational axis and the line-of-sight from Earth is significantly larger for YZ CMi and EV Lac compared to AD Leo (Table S1).

Figure S4(a) presents possible scenarios that may explain the field **with opposite polarities at different heights**. We see two magnetic field lines originating from the same region but reaching different locations. For one large-scale magnetic loop, if the direction of the loop sharply changes with height, the measured longitudinal field at different heights can have different polarities. These scenarios may explain the different strengths of average longitudinal magnetic fields at different heights, and the sign of the middle chromospheric field can be opposite to that of the photospheric field. As a test, we applied the photospheric field of AD Leo in Potential Field Source Surface (PFSS) modeling[7] to extrapolate the large-scale field at a typical height of the chromosphere of $1.003R_*$ according to the Sun. As shown in Figure S5, with the inclination of $i = 20°$ and $60°$, although the radial field has very tiny variation, it is still possible to result in a decrease of $\langle B_l \rangle$ or even an opposite sign. We also made simple simulations (details in Supplement Text 1C) to reproduce the observed anti-correlations between layers. Note that the chromosphere should be much thinner than shown in the figures, meaning that large-scale magnetic loops are highly curved and lie very close to the stellar surfaces. Although actual situations are much more complex, these toy models can already explain our observed field variation with height, highlighting the strongly varying magnetic topologies with height.

Figures S6 to S8 present correlation analyses of all our measurements of longitudinal fields between different atmospheric layers, along with corresponding linear fittings for each correlation. Although the correlations between longitudinal fields in different layers vary within each epoch, there is an overall global correlation with all observations. For instance, in panel (a) of Figure S8, the photospheric magnetic field strengths of EV Lac in 2016 are weak but aligned with the linear fitting derived from the 2007 measurements, which exhibits a broader range of field variations. Similarly, the single observation of YZ CMi in 2009 fits the trend observed in 2007. Even though the field strength of AD Leo is relatively stable, a universal slope can still be observed in Figure S6 (c). These linear relationships suggest an intrinsic connection between the large-scale magnetic field structures from layer to layer, e.g., sharing the same magnetic loops. The numerical Pearson coefficient r and its two-tailed p-value are listed in Table S5, indicating a highly significant correlation for all data between photospheric and chromospheric fields, especially for YZ CMi and EV Lac.

1C. Complexity of the large-scale magnetic field structure

The complexity of the large-scale magnetic field close to the surface in our work is evaluated by the correlation between layers. **Zeeman-Doppler Imaging (ZDI) reconstruction of the 2-D chromospheric magnetic field map can potentially provide information on field complexity. It is unclear whether the small number of available chromospheric lines can be used to create a reliable map. Nevertheless, some ideas from ZDI can still be useful for testing the field complexity.** For a model of magnetic field topology, we can define the complexity of the large-scale magnetic field by the degree (ℓ) of the spherical harmonics decomposition of the field [8]. The radial field is defined by $B_r\ (\theta, \phi) = \Sigma_{\ell=1}^{L} \Sigma_{m=0}^{\ell} \mathrm{Re}[\alpha_{\ell m} Y_{\ell m}(\theta, \phi)]$, where (θ, ϕ) are the colatitude and longitude on the stellar surface, $Y_{\ell m} = c_{\ell m} P_{\ell m}(\cos\theta) e^{im\phi}$ with $c_{\ell m} = \sqrt{(2\ell + 1(\ell - m)!)/(4\pi(\ell + m)!)}$ and $P_{\ell m}$ the associated Legendre polynomial. m gives the order of the spherical harmonics mode and describes the azimuthal variation or symmetry of the field. In practice, $\alpha_{\ell m}$ is a complex coefficient corresponding to the radial poloidal field with specific ℓ and m. We examined dipole ($\ell = 1$), quadrupole ($\ell = 2$), and octupole ($\ell = 3$) fields, constructed from a photospheric field with slight asymmetry (give equal energy to m=0 and $m > 0$) and extrapolated to the upper layers via Potential Field Source Surface (PFSS) modeling[7]. We set an inclination of $i = 40°$ (Figure S9), the correlation between the B_ℓ of the photosphere and a layer outside at 1.05 R_* is high with $\ell = 1$ and 2, but moderate for ℓ=3. These extrapolations indicate that a more complex magnetic field structure results in a lower correlation between magnetic fields at different layers. Our complexity ranking for the targets is as follows: AD Leo is the most complex, YZ CMi is the most organized, and EV Lac is intermediate. These simulations can also be used to explain the **opposite polarities** and anti-correlation between different layers in our observations. In Figure S9 (b), **opposite polarity** frequently happens, indicating that the quadrupole of the magnetic field is enough to generate this phenomenon. In Figure S9 (c), we show a possible situation with an anti-correlated pattern together with **opposite polarities between the surface and** outer layers, suggesting that the octupole mode can account for both two phenomena. Note that the solar chromosphere is located at only around 0.3% $R_\odot$ above the surface, which is about an order of magnitude lower than the layer we take in the simulation. This is because the topology of the extrapolated field with PFSS does not vary too much from the surface to such a low height, resulting in a correlation coefficient value close to 1. The magnetic loops in the model (black lines in the middle panels of Figure S9) need to be at a higher layer to achieve the degree of bending to reproduce the phenomena.

1D. Flare Frequency Distributions

Flare Frequency Distributions (FFDs) describe the relationship between the occurring frequency of stellar flares and their energy or intensity. Specifically, FFDs quantify how often flares of varying energies occur over a given period. We extracted the flares from TESS Sector 1-57, with the state-of-the-art method dedicated to TESS flare detection developed by [9]. Figure S9 presents FFDs for our three targets, using data from the Transiting Exoplanet Survey Satellite (TESS) from 2018 to 2024, including three sectors for each star. We see a trend that stars with more low-energy flares have fewer high-energy flares. Figure S9 shows that stars with more complex fields tend to exhibit more high-energy flares and fewer low-energy ones. In the solar case, it is well-known that more complex magnetic field structures in active regions produce more flares[10], which is similar to the occurrence of high-energy flares in our observations. Fewer low-energy flares in the situation of more complex fields can be attributed to the rich small-scale field on the surface of these M dwarfs, which can convert the low-energy flares to increased magnetic dissipation and prune the FFD.

References

[1] Fuhrmeister, B., Schmitt, J. H. M. M. & Hauschildt, P. H. PHOENIX model chromospheres of mid- to late-type M dwarfs. *Astronomy and Astrophysics* **439**, 1137–1148 (2005).

[2] Hintz, D. *et al.* Modeling the Chromosphere and Transition Region of Planet-hosting Star GJ 436. *The Astrophysical Journal* **954**, 73 (2023).

[3] Mathur, H., Nagaraju, K., Joshi, J. & de la Cruz Rodríguez, J. Do Hα Stokes V Profiles Probe the Chromospheric Magnetic Field? An Observational Perspective. *The Astrophysical Journal* **946**, 38 (2023).

[4] Morin, J. *et al.* Large-scale magnetic topologies of mid M dwarfs. *Monthly Notices of the Royal Astronomical Society* **390**, 567–581 (2008).

[5] Bellotti, S. *et al.* Monitoring the large-scale magnetic field of AD Leo with SPIRou, ESPaDOnS, and Narval. Towards a magnetic polarity reversal? *Astronomy and Astrophysics* **676**, A56 (2023).

[6] Bellotti, S. *et al.* Long-term monitoring of large-scale magnetic fields across optical and near-infrared domains with ESPaDOnS, Narval and SPIRou. The cases of EV Lac, DS Leo, and CN Leo. *arXiv e-prints* arXiv:2403.08590 (2024).

[7] Stansby, D., Yeates, A. & Badman, S. pfsspy: A Python package for potential field source surface modelling. *The Journal of Open Source Software* **5**, 2732 (2020).

[8] Donati, J. F. *et al.* The surprising magnetic topology of τ Sco: fossil remnant or dynamo output? *MNRAS* **370**, 629–644 (2006).

[9] Xing, K. *et al.* Flare Hunting in Hot Subdwarf and White Dwarf Stars from Cycles 1–5 of TESS Photometry. *ApJS* **271**, 57 (2024).

[10] Wood, B. E. *et al.* New Observational Constraints on the Winds of M dwarf Stars. *ApJ* **915**, 37 (2021).

[11] Engle, S. G. Living with a Red Dwarf: X-Ray, UV, and Ca II Activity-Age Relationships of M Dwarfs. *ApJ* **960**, 62 (2024).

[12] Kochukhov, O., Hackman, T., Lehtinen, J. J. & Wehrhahn, A. Hidden magnetic fields of young suns. *A&A* **635**, A142 (2020).

2. Extended Data: Figures

S1. Modeling the photospheric component of Ca IRT in Stokes I & V

(a) A Lorentzian model (blue curve) is used to fit the broad wing (20-100 km/s) of the Ca IRT LSD Stokes *I* profile (black dots). (c) The residual I profile (subtraction of the Lorentzian model from the Stokes I profile) is used for $\langle B_{\rm cM} \rangle$ estimation. (b) The corresponding circular polarization model (blue curve) with fixed $\langle B_{\rm p} \rangle$. The black dots with error bars are the measured Stokes V profile. (d) The residual V profile (subtraction of the circular polarization model from the Stokes V profile) is used for $\langle B_{\rm cM} \rangle$ estimation.

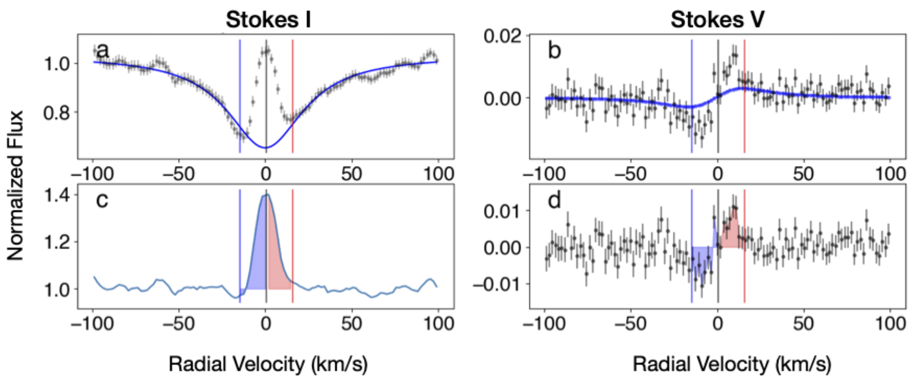

S2. An example of the Stokes-I and V profiles of YZ CMi from the observation on 2007-12-29.

Blue and red vertical lines indicate the positions of emission peaks Hα2v and Hα2r.

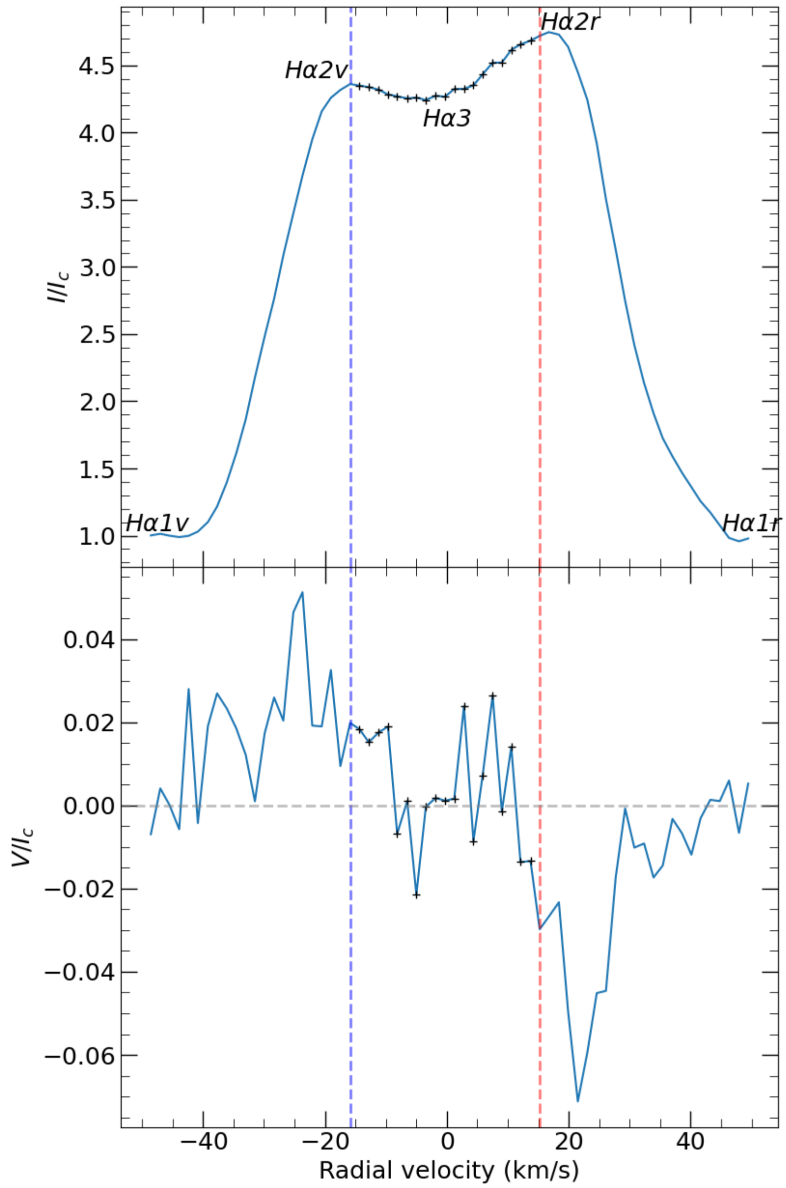

S3. Repeating pattern of measurements in the selected epoch of YZ CMi. The measurements are the same as in Fig. 2; the color shows the day difference from HJD = 2454500. For reference, the solid line represents the fit of the data using a double sine function.

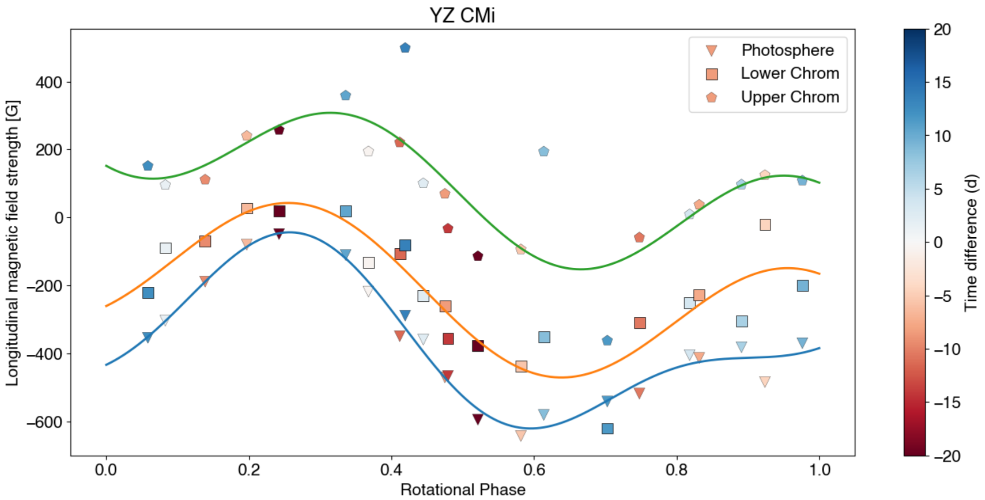

***S4. A cartoon showing a possible scenario of magnetic field* with opposite polarities at different heights**

For example, we take a minimized magnetic field structure on the surface of AD Leo. Two magnetic field lines originate from region A and then reach B and C, respectively. The layers with red, orange and blue colors indicate the photosphere, lower chromosphere and middle chromosphere, respectively. The angle between the line-of-sight and rotation axis is set to be $i = 20°$, with the shadow part of the star invisible for observation. The visible parts of magnetic field lines are shown in the same colors as layers. The arrows with different colors indicate the polarities of the measured magnetic fields at corresponding layers.

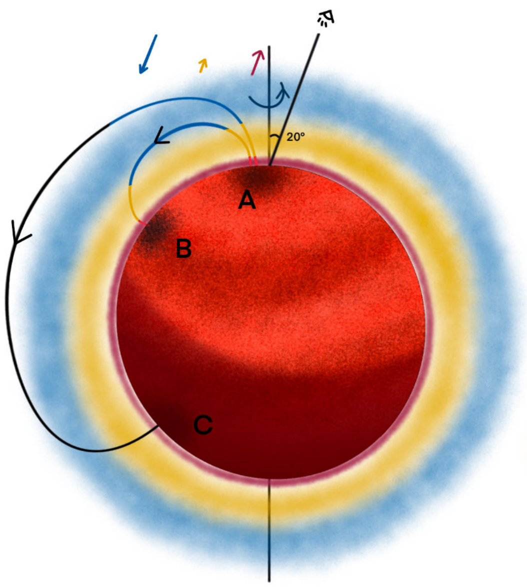

S5. PFSS modeling experiment for AD Leo

We take the radial field of AD Leo in (a) for PFSS modeling, and obtain the extrapolated field at $1.003R_*$ in (b). The corresponding line-of-sight mean field $\langle B_\mathrm{l} \rangle$ vs. rotation phase with different inclinations of $i = 20°$ and $60°$ are shown in (c) and (d), respectively.

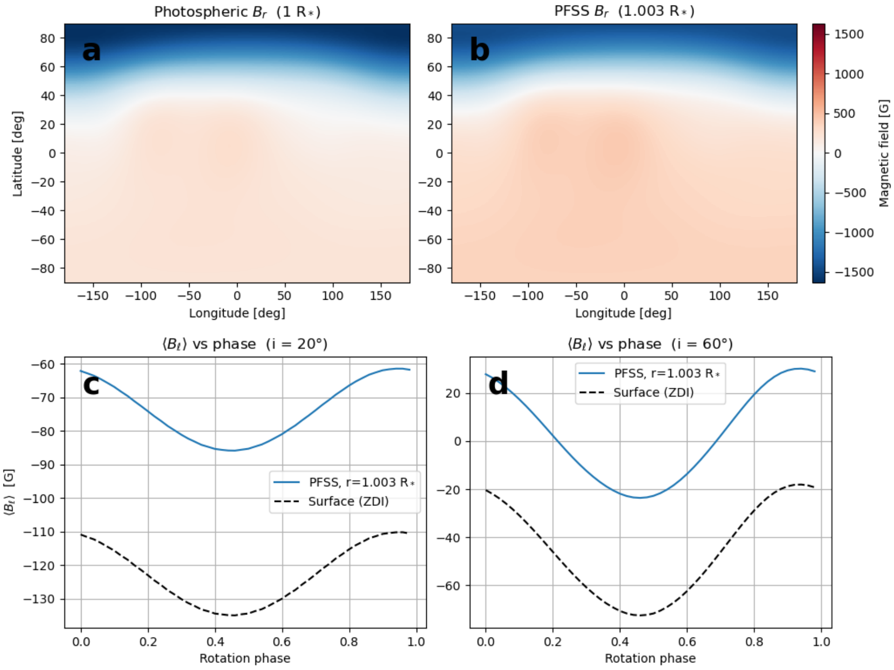

S6. Correlation among photospheric, lower and middle chromospheric longitudinal magnetic fields for AD Leo

(a) The correlation between $\langle B_{\mathrm{p}}\rangle$ and $\langle B_{\mathrm{cL}}\rangle$ for all data. The original values and corresponding uncertainties can be found in Table S4. Each epoch legend has the start date and is shown with a different color. For the epochs with over three observations, a linear regression is presented by a line with the same color. A linear regression for all observations is presented with the gray dashed line. (b,c) Same as panel (a), but for the correlation between $\langle B_{\mathrm{cM}}\rangle$ and $\langle B_{\mathrm{p}}\rangle$ (b), $\langle B_{\mathrm{cL}}\rangle$ (c), respectively. The corresponding Pearson correlation coefficient for each linear fitting is presented in the table in the upper-right panel with the same color selection as the other panel for each epoch.

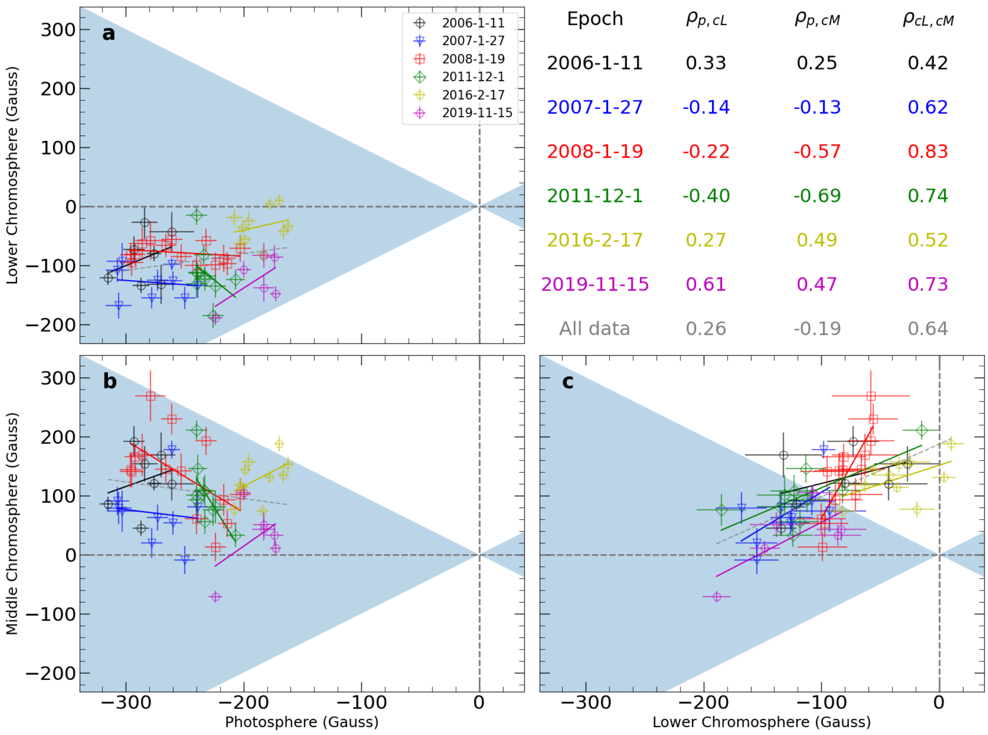

Epoch	$\rho_{p,cL}$	$\rho_{p,cM}$	$\rho_{cL,cM}$
2006-1-11	0.33	0.25	0.42
2007-1-27	-0.14	-0.13	0.62
2008-1-19	-0.22	-0.57	0.83
2011-12-1	-0.40	-0.69	0.74
2016-2-17	0.27	0.49	0.52
2019-11-15	0.61	0.47	0.73
All data	0.26	-0.19	0.64

S7. Same as Fig. S6 but for YZ CMi.

The original values and corresponding uncertainties can be found in Table S2.

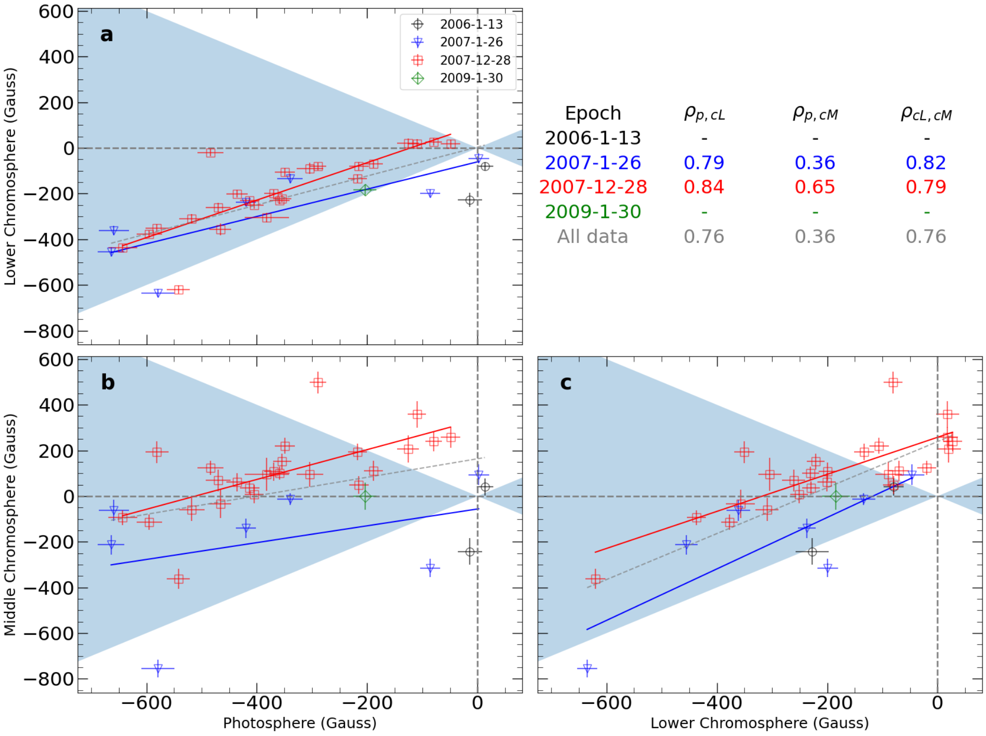

S8. Same as Fig. S6, but for EV Lac.

The original values and corresponding uncertainties can be found in Table S3.

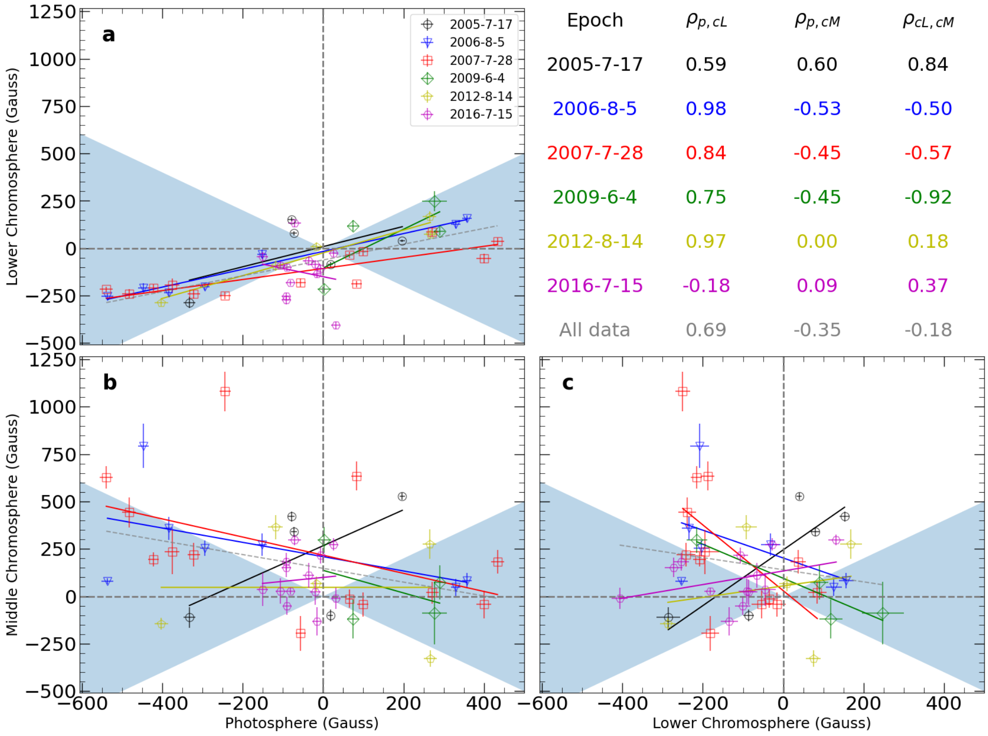

Epoch	$\rho_{p,cL}$	$\rho_{p,cM}$	$\rho_{cL,cM}$
2005-7-17	0.59	0.60	0.84
2006-8-5	0.98	-0.53	-0.50
2007-7-28	0.84	-0.45	-0.57
2009-6-4	0.75	-0.45	-0.92
2012-8-14	0.97	0.00	0.18
2016-7-15	-0.18	0.09	0.37
All data	0.69	-0.35	-0.18

S9. PFSS modeling with $\ell = 1$, 2, and 3

Panels on the left show radial field distribution on the photosphere and corresponding PFSS modeling results. The blue and red areas indicate the strengths of the magnetic field, with the color bar shown in Gauss. Blue and red lines represent the negative- and positive-polarity open field lines, respectively. The black lines are closed field lines. Panels on the right present the variation of the average line-of-sight magnetic field strength of the photosphere (black dashed lines, $R = 1R_*$) and a higher layer (blue lines, $R = 1.05R_*$) as a function of the rotation phase. The corresponding correlation coefficients ρ between the magnetic fields of the two layers are presented on the left panels.

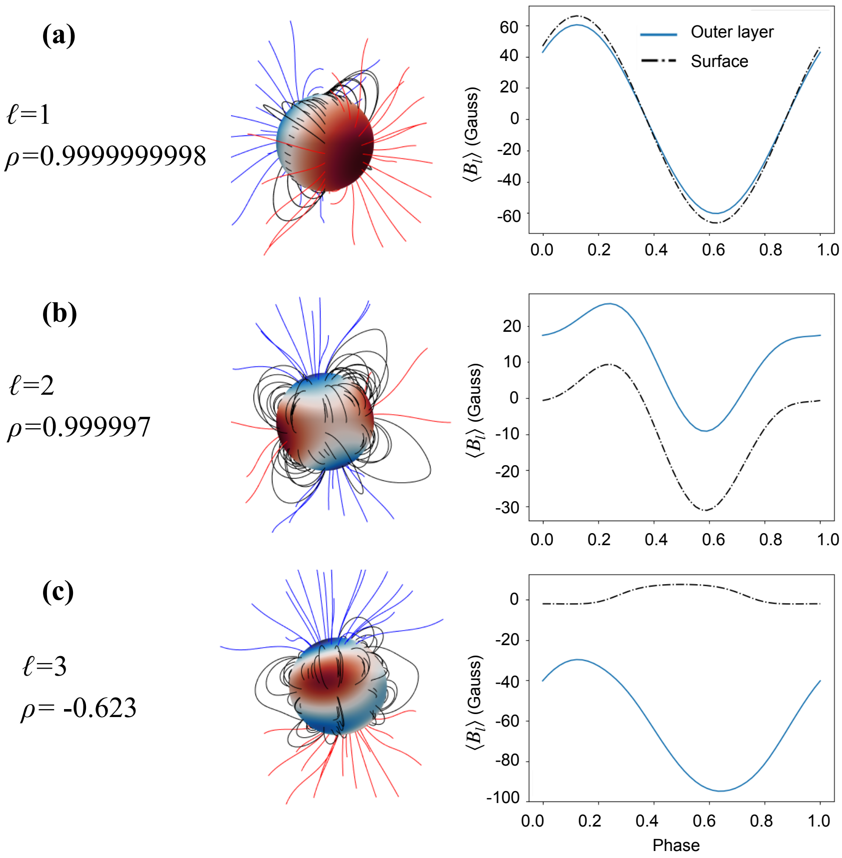

S10. Cumulative Flare Frequency Distributions of the three stars, derived from TESS observations.

The corresponding slope (red lines) β gives the power-law fitting for the middle-to-high energy part ($10^{32} - 10^{33.5}$ erg), the value can be found in Table S1.

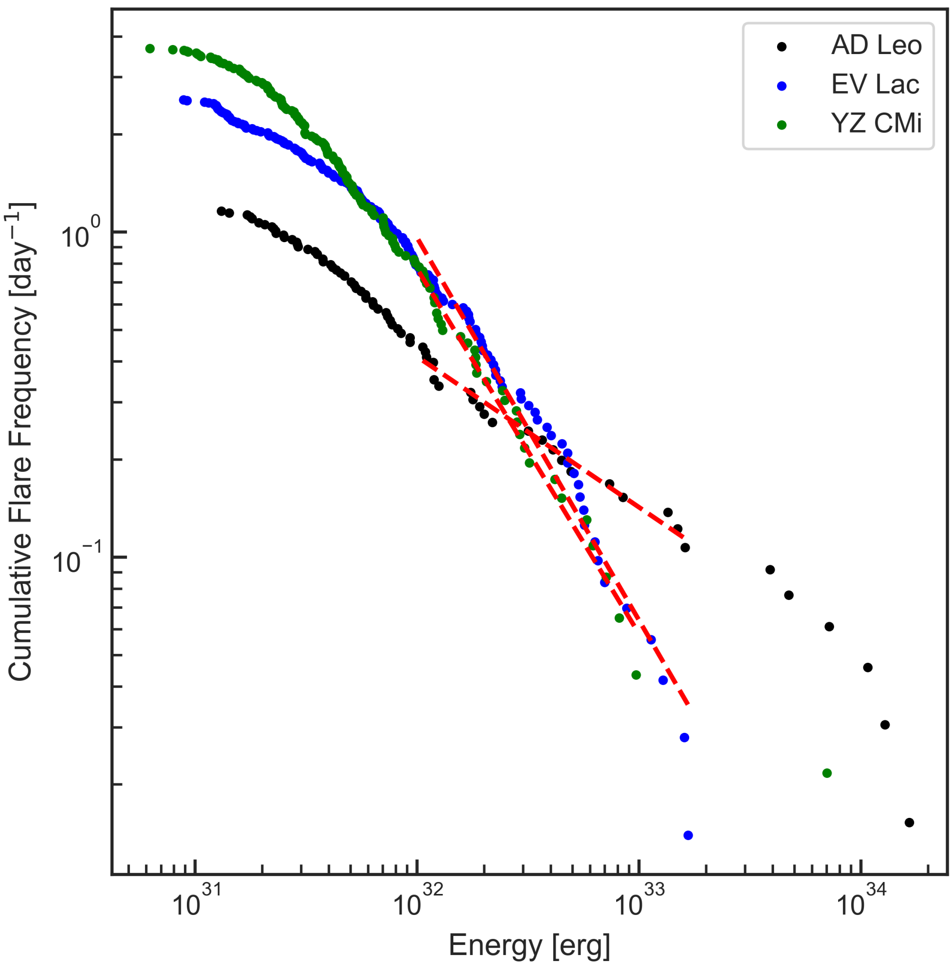

3. Extended Data: Tables

S1. Stellar parameters of the observed M-dwarfs

Most of the parameters are taken from [4], including stellar mass, radius, spectral type, period, radial velocity (RV), $v\sin\, i$, and the inclination angle (INCL) between the rotational axis and the line-of-sight from Earth. Stellar age are taken from [11], the percentage of large-scale field $\langle B_V \rangle / \langle B_I \rangle$ are taken from [12]. β gives the slope of power-law fitting of FFD (Fig. S10).

Values	AD Leo	YZ CMi	EV Lac
Mass ($M_\odot$)	0.42	0.31	0.32
Radius ($R_\odot$)	0.38	0.29	0.30
Spec Type	M3	M4.5	M3.5
log(Age) [yr]	-0.764	-0.092	-0.052
Period (d)	2.22	2.77	4.378
RV (km/s)	12.3	26.6	-1.5
$v\sin\, i$ (km s^{-1})	3.0	5.2	4.0
INCL (°)	20	60	60
$\langle B_V \rangle / \langle B_I \rangle$	5.8%	13.3%	10.2%
β	-0.79 ± 0.09	-1.024 ± 0.0016	-0.67 ± 0.09

S2. Journal of observations for YZ CMi.

This is the information of the measurements plotted in Figure 2. Columns 1-3, respectively, list the observation UT date, the heliocentric Julian date (HJD), and the rotational phase calculated from the ephemeris in the Method section. Column 4 presents the total exposure time of the Stokes V sequence. Columns 5–7 provide the peak signal-to-noise ratio per 1.8 km s^{-1} velocity bin measured in the unprocessed spectra for the Hα line, the Ca II infrared triplet, and the full multi-line LSD profile. Columns 8–10 list the disk-integrated longitudinal magnetic field derived with the center-of-gravity method for the photosphere ($\langle B_{\rm p}\rangle$), the lower chromosphere ($\langle B_{\rm cL}\rangle$, from H$\alpha$), and the middle chromosphere ($\langle B_{\rm cM}\rangle$, from Ca IRT), all in gauss. Epoch-by-epoch Pearson correlation coefficients between these three layers are compiled in Table S5.

ObsDate	JD	Phase	ExpTime (s)	SNR Hα	SNR Ca IRT	SNR LSD	$\langle B_{\rm p}\rangle$ (Gauss)	$\langle B_{\rm cL}\rangle$ (Gauss)	$\langle B_{\rm cM}\rangle$ (Gauss)
2006-1-13	2453748.9279	0.4108	1200	75	263	1918	-14 ± 22	-227 ± 30	-242 ± 57
2006-2-7	2453773.9434	0.4416	1800	127	431	2972	13 ± 15	-80 ± 18	40 ± 38
2007-1-26	2454127.4387	0.0573	3600	131	315	2766	-340 ± 23	-134 ± 21	-13 ± 26
2007-1-27	2454128.4794	0.4330	3600	139	367	3289	-664 ± 24	-455 ± 20	-213 ± 42
2007-1-29	2454130.474	0.1531	3600	183	439	4106	-420 ± 18	-237 ± 16	-141 ± 42
2007-2-1	2454133.5001	0.2455	3600	143	346	3002	-579 ± 30	-635 ± 18	-755 ± 38
2007-2-3	2454135.4944	0.9655	3600	150	364	3227	-86 ± 18	-199 ± 19	-315 ± 40
2007-2-4	2454136.462	0.3148	3600	140	362	3230	-659 ± 27	-361 ± 21	-63 ± 46
2007-2-8	2454140.4775	0.7644	3600	137	333	2959	2 ± 19	-46 ± 22	94 ± 46
2007-12-28	2454462.6263	0.0637	4800	157	378	3335	-215 ± 18	-80 ± 19	49 ± 39
2007-12-29	2454463.6563	0.4355	4800	177	445	4183	-436 ± 19	-201 ± 17	61 ± 40
2007-12-31	2454465.6705	0.1626	3600	122	307	2708	-126 ± 20	20 ± 22	206 ± 59
2008-1-1	2454466.6638	0.5212	4400	170	456	4079	-595 ± 23	-377 ± 15	-114 ± 34
2008-1-3	2454468.6611	0.2423	4400	149	342	3103	-49 ± 18	18 ± 19	257 ± 45
2008-1-20	2454485.9373	0.4792	880	104	347	2806	-466 ± 20	-357 ± 26	-33 ± 62
2008-1-22	2454488.52	0.4116	4800	156	386	3643	-349 ± 18	-106 ± 18	220 ± 35
2008-1-23	2454489.4511	0.7477	4800	143	355	3184	-518 ± 23	-309 ± 21	-59 ± 50
2008-1-24	2454490.5339	0.1386	4800	161	386	3593	-189 ± 17	-70 ± 18	111 ± 43
2008-1-25	2454491.4654	0.4749	4800	138	352	3192	-470 ± 22	-261 ± 21	69 ± 48
2008-1-26	2454492.4536	0.8316	4800	179	431	4008	-413 ± 18	-229 ± 16	37 ± 28
2008-1-27	2454493.4657	0.1970	4800	176	422	3946	-80 ± 15	27 ± 17	239 ± 42
2008-1-28	2454494.5307	0.5815	4800	139	390	3296	-643 ± 26	-437 ± 17	-94 ± 32
2008-1-29	2454495.4789	0.9238	4800	163	399	3474	-484 ± 24	-20 ± 17	124 ± 31
2008-2-2	2454499.4786	0.3677	4800	157	379	3412	-218 ± 17	-133 ± 18	194 ± 37
2008-2-4	2454501.4594	0.0828	4800	114	300	2432	-304 ± 24	-89 ± 24	95 ± 54
2008-2-5	2454502.4614	0.4446	4800	163	406	3748	-359 ± 18	-230 ± 16	100 ± 29
2008-2-6	2454503.4964	0.8182	4800	171	430	3948	-405 ± 17	-251 ± 16	8 ± 40
2008-2-9	2454506.4677	0.8909	4800	62	192	1397	-382 ± 40	-304 ± 21	96 ± 72
2008-2-11	2454508.4698	0.6136	4800	156	426	3904	-581 ± 21	-350 ± 18	193 ± 48
2008-2-12	2454509.4742	0.9763	4800	173	432	3949	-370 ± 17	-199 ± 17	108 ± 40
2008-2-13	2454510.4699	0.3357	4800	144	354	3207	-110 ± 17	18 ± 21	358 ± 58
2008-2-14	2454511.4864	0.7027	4800	152	394	3636	-542 ± 21	-620 ± 18	-362 ± 44
2008-2-15	2454512.4716	0.0583	4800	177	426	3950	-354 ± 17	-221 ± 16	151 ± 34
2008-2-16	2454513.4711	0.4192	4800	183	442	4098	-289 ± 15	-81 ± 17	498 ± 48
2009-1-30	2454862.4925	0.4197	4800	118	299	2594	-204 ± 21	-184 ± 25	-1 ± 60

S3

Same as Table S2, but for EV Lac.

ObsDate	JD	Phase	ExpTime (s)	SNR Hα	SNR Ca IRT	SNR LSD	$\langle B_{\rm p}\rangle$ (Gauss)	$\langle B_{\rm cL}\rangle$ (Gauss)	$\langle B_{\rm cM}\rangle$ (Gauss)
2005-7-17	2453569.1119	0.0392	4800	289	946	9180	197 ± 7	40 ± 7	528 ± 20
2005-8-23	2453606.1478	0.4949	800	130	365	3245	-333 ± 15	-286 ± 29	-111 ± 54
2005-9-18	2453631.9065	0.3759	3000	264	718	6646	18 ± 7	-86 ± 13	-100 ± 31
2005-9-18	2453631.9447	0.3846	3000	259	705	6537	-79 ± 8	153 ± 12	421 ± 26
2005-9-18	2453631.9828	0.3933	3000	286	729	7292	-73 ± 7	80 ± 11	341 ± 24
2006-8-5	2453953.0731	0.7016	1200	176	551	5081	-537 ± 15	-253 ± 15	80 ± 15
2006-8-7	2453955.0663	0.1567	1200	201	557	5313	358 ± 12	157 ± 18	83 ± 40
2006-8-8	2453956.06	0.3836	1600	218	674	6390	-385 ± 11	-234 ± 18	359 ± 61
2006-8-9	2453957.0597	0.6118	920	169	491	4629	-448 ± 13	-208 ± 24	794 ± 118
2006-8-10	2453958.0723	0.8430	1000	165	484	4467	-295 ± 12	-204 ± 19	254 ± 40
2006-8-11	2453959.0728	0.0714	1000	189	514	4818	330 ± 12	126 ± 20	48 ± 45
2006-8-12	2453960.0761	0.3005	1000	175	455	4272	-152 ± 12	-31 ± 24	272 ± 59
2007-7-28	2454309.5464	0.0882	3600	283	549	5999	66 ± 9	-34 ± 15	-13 ± 48
2007-7-29	2454310.5661	0.3210	3600	229	558	6118	-423 ± 13	-208 ± 16	195 ± 38
2007-7-30	2454311.5937	0.5556	3600	198	515	5562	-540 ± 16	-216 ± 14	627 ± 59
2007-7-31	2454312.5937	0.7840	2400	202	410	4386	83 ± 13	-188 ± 17	635 ± 76
2007-8-1	2454313.5958	0.0127	2400	169	352	3688	272 ± 16	85 ± 23	19 ± 57
2007-8-3	2454315.6018	0.4707	2400	171	402	4304	-483 ± 17	-239 ± 22	443 ± 80
2007-8-4	2454316.5998	0.6986	2400	201	418	4441	-244 ± 14	-250 ± 18	1081 ± 105
2007-8-5	2454317.6712	0.9432	2400	162	356	3649	400 ± 18	-54 ± 24	-43 ± 73
2007-8-10	2454322.5952	0.0674	2400	189	374	3930	99 ± 14	-16 ± 23	-43 ± 64
2007-8-11	2454323.5977	0.2963	2400	140	307	3109	-376 ± 18	-195 ± 36	234 ± 117
2007-8-15	2454327.5882	0.2074	2400	188	396	4258	-322 ± 15	-242 ± 23	220 ± 63
2007-8-18	2454330.5813	0.8907	2400	184	414	4465	434 ± 16	37 ± 19	182 ± 62
2007-8-18	2454331.5149	0.1039	2400	218	424	4577	-56 ± 12	-182 ± 22	-196 ± 91
2009-6-4	2454986.5995	0.6666	2400	163	384	3862	290 ± 14	90 ± 23	74 ± 90
2009-6-12	2454994.6321	0.5005	2400	146	320	3139	3 ± 17	-215 ± 26	298 ± 68
2009-6-13	2454995.5842	0.7179	2400	79	176	1558	277 ± 31	248 ± 52	-88 ± 165
2009-8-15	2455059.3898	0.2853	2400	166	354	3429	74 ± 15	119 ± 29	-120 ± 102
2012-8-14	2456153.6218	0.1100	2400	155	351	3644	-403 ± 17	-287 ± 19	-145 ± 32
2012-8-15	2456155.5086	0.5408	2400	138	316	3249	265 ± 17	169 ± 27	277 ± 78
2012-8-16	2456156.4857	0.7639	2400	131	287	2910	-119 ± 18	-92 ± 26	365 ± 64
2012-8-17	2456157.5074	0.9971	2400	155	340	3534	267 ± 16	75 ± 19	-328 ± 44
2012-8-22	2456161.6002	0.9315	2400	174	375	3946	-17 ± 15	10 ± 19	67 ± 39
2016-7-15	2457584.5642	0.8092	2400	178	418	4173	-106 ± 12	-90 ± 21	28 ± 68
2016-7-16	2457585.5742	0.0398	2400	163	370	3624	-71 ± 16	132 ± 20	297 ± 28
2016-7-18	2457587.6371	0.5108	2400	167	398	3947	-92 ± 12	-273 ± 22	152 ± 51
2016-7-19	2457588.5683	0.7234	2400	188	444	4498	-16 ± 11	-134 ± 21	-133 ± 74
2016-7-20	2457589.5501	0.9475	2400	154	360	3554	-151 ± 14	-45 ± 26	35 ± 87
2016-7-21	2457590.5214	0.1693	2400	174	398	4001	26 ± 12	-27 ± 18	274 ± 33
2016-7-26	2457595.5856	0.3255	2400	180	433	4371	-92 ± 11	-254 ± 19	182 ± 47
2016-7-27	2457596.6157	0.5607	2400	185	447	4538	31 ± 11	-407 ± 20	-12 ± 56
2016-7-28	2457597.5553	0.7752	2400	193	442	4472	-90 ± 11	-101 ± 19	-50 ± 49
2016-8-3	2457603.5542	0.1448	2400	173	369	3902	-20 ± 13	-86 ± 22	22 ± 67
2016-8-7	2457608.4675	0.2665	2400	205	462	4721	-82 ± 12	-182 ± 14	28 ± 18
2016-8-9	2457609.5398	0.5114	2400	182	413	4222	-6 ± 12	-106 ± 19	215 ± 43
2016-8-12	2457612.5894	0.2076	2400	154	368	3629	-36 ± 14	-66 ± 24	111 ± 66

S4

Same as Table S2, but for AD Leo.

ObsDate	JD	Phase	ExpTime (s)	SNR Hα	SNR Ca IRT	SNR LSD	$\langle B_p \rangle$ (Gauss)	$\langle B_{cL} \rangle$ (Gauss)	$\langle B_{cM} \rangle$ (Gauss)
2006-1-11	2453747.0876	0.5980	1200	105	342	2381	-261 ± 19	-43 ± 33	120 ± 28
2006-1-13	2453748.8868	0.4085	1200	149	414	3809	-270 ± 12	-132 ± 33	169 ± 38
2006-2-13	2453780.0705	0.4552	1200	174	509	4417	-284 ± 11	-27 ± 28	154 ± 30
2006-6-9	2453895.8047	0.5877	2400	218	619	6127	-293 ± 9	-73 ± 22	192 ± 26
2006-6-10	2453896.8124	0.0416	2400	298	985	9395	-287 ± 7	-134 ± 13	45 ± 13
2006-6-11	2453897.8005	0.4867	2400	315	1036	10092	-276 ± 6	-80 ± 13	121 ± 12
2006-6-12	2453898.7785	0.9272	2400	280	983	9386	-315 ± 7	-121 ± 12	86 ± 12
2007-1-27	2454127.5975	0.9989	2400	178	382	4200	-303 ± 13	-93 ± 31	74 ± 35
2007-1-28	2454128.6088	0.4544	2400	266	549	6336	-239 ± 9	-134 ± 21	81 ± 27
2007-1-29	2454129.5717	0.8881	2400	244	543	6281	-307 ± 10	-108 ± 20	91 ± 24
2007-1-30	2454130.6084	0.3551	2400	301	662	7855	-260 ± 8	-126 ± 16	54 ± 20
2007-2-2	2454133.6312	0.7167	2400	260	591	6835	-278 ± 9	-155 ± 18	20 ± 25
2007-2-3	2454134.6112	0.1582	2400	259	549	6345	-273 ± 9	-125 ± 18	63 ± 22
2007-2-4	2454135.6217	0.6134	2400	266	565	6542	-250 ± 9	-155 ± 19	-9 ± 24
2007-2-5	2454136.5925	0.0507	2400	220	470	5497	-306 ± 11	-168 ± 22	79 ± 27
2007-6-25	2454276.7715	0.1944	4000	330	998	8904	-261 ± 7	-98 ± 10	178 ± 15
2008-1-19	2454485.5177	0.2242	3200	206	436	4892	-286 ± 11	-63 ± 28	169 ± 36
2008-1-24	2454489.5683	0.0488	2400	253	551	6381	-253 ± 9	-85 ± 21	142 ± 30
2008-1-27	2454492.5379	0.3864	2400	259	582	6896	-296 ± 9	-82 ± 20	144 ± 30
2008-1-28	2454493.5486	0.8417	2400	262	542	6208	-224 ± 9	-99 ± 21	13 ± 24
2008-1-30	2454495.5611	0.7482	2400	226	457	5231	-217 ± 10	-88 ± 23	93 ± 27
2008-2-3	2454499.5675	0.5529	2400	247	524	6047	-266 ± 9	-66 ± 20	145 ± 25
2008-2-5	2454501.5473	0.4447	2400	235	491	5606	-295 ± 10	-95 ± 23	141 ± 27
2008-2-6	2454502.5475	0.8953	2400	277	561	6570	-214 ± 8	-97 ± 20	53 ± 23
2008-2-10	2454506.5576	0.7016	2400	271	573	6654	-232 ± 9	-58 ± 20	193 ± 24
2008-2-12	2454508.5516	0.5998	2400	247	547	6259	-261 ± 9	-56 ± 21	230 ± 26
2008-2-13	2454509.5564	0.0524	2400	258	567	6225	-240 ± 10	-100 ± 21	61 ± 26
2008-2-14	2454510.5523	0.5010	2400	181	375	4115	-279 ± 13	-58 ± 33	269 ± 43
2008-2-15	2454511.5694	0.9592	2400	261	522	5988	-203 ± 9	-71 ± 23	102 ± 28
2008-2-16	2454512.5537	0.4026	2400	255	576	6675	-292 ± 9	-81 ± 19	166 ± 22
2011-12-1	2455896.756	0.9171	2400	212	488	5767	-240 ± 9	-131 ± 24	101 ± 34
2012-1-8	2455934.6407	0.9823	2400	259	611	7145	-239 ± 8	-113 ± 17	146 ± 24
2012-1-9	2455935.6765	0.4489	2400	256	617	7149	-234 ± 8	-82 ± 17	109 ± 22
2012-1-10	2455936.605	0.8671	2400	222	530	6081	-233 ± 9	-123 ± 20	108 ± 27
2012-1-11	2455937.7575	0.3863	2400	218	530	5959	-240 ± 9	-15 ± 16	211 ± 16
2012-1-12	2455938.6659	0.7955	2400	260	661	7730	-240 ± 7	-112 ± 17	93 ± 21
2012-1-13	2455939.6031	0.2176	2400	215	529	6034	-226 ± 9	-185 ± 21	76 ± 27
2012-1-14	2455940.6416	0.6854	2400	261	615	7145	-207 ± 8	-124 ± 17	33 ± 20
2012-1-15	2455941.6411	0.1356	2400	242	587	6902	-233 ± 8	-118 ± 16	56 ± 21
2012-1-16	2455942.6256	0.5791	2400	233	534	6182	-224 ± 9	-135 ± 20	81 ± 28
2016-2-17	2457435.7957	0.1782	2400	388	1467	7691	-199 ± 5	-56 ± 10	144 ± 10
2016-2-18	2457436.8831	0.6681	2400	381	1314	7696	-170 ± 4	10 ± 11	188 ± 13
2016-2-23	2457441.8954	0.9259	2400	392	1443	7920	-201 ± 5	-36 ± 10	114 ± 9
2016-2-24	2457443.0074	0.4268	2400	409	1470	8079	-178 ± 4	4 ± 10	131 ± 10
2016-2-29	2457447.9103	0.6353	1200	311	1072	5872	-166 ± 5	-42 ± 14	135 ± 14
2016-3-1	2457449.0011	0.1266	1200	270	928	5105	-196 ± 6	-25 ± 17	157 ± 15
2016-3-2	2457449.9154	0.5385	1200	308	1057	5844	-162 ± 5	-34 ± 13	153 ± 13
2016-3-3	2457450.8328	0.9517	1200	290	1027	5592	-203 ± 6	-63 ± 14	118 ± 12
2016-4-17	2457495.8253	0.2186	2400	238	920	4388	-208 ± 7	-19 ± 15	77 ± 13
2016-4-20	2457498.7442	0.5334	2400	349	1317	6999	-184 ± 5	-82 ± 12	74 ± 11
2019-11-15	2458803.0577	0.0620	1200	280	1059	8882	-224 ± 6	-189 ± 12	-71 ± 10
2019-11-16	2458804.0967	0.5300	1200	275	1003	8396	-200 ± 6	-107 ± 14	105 ± 13
2019-11-19	2458807.089	0.8779	1200	180	647	4350	-183 ± 10	-83 ± 21	43 ± 19
2019-11-19	2458807.1062	0.8857	1200	190	596	4955	-183 ± 9	-138 ± 23	51 ± 21
2019-11-19	2458807.1223	0.8929	1200	215	688	5753	-174 ± 8	-86 ± 20	33 ± 18
2019-11-21	2458809.1547	0.8084	1200	317	1048	9045	-173 ± 5	-148 ± 13	11 ± 13

S5. Epoch-by-epoch statistical information of each star

For each observing epoch defined in Tables S2–S4, the correlations between the disk-integrated longitudinal magnetic fields measured in the three atmospheric layers. Column 1 gives the UTC start date of the epoch and Column 2 its end date; Column 3 lists the number of individual Stokes V spectra acquired during that epoch (ObsCount). Columns 4–6 provide the Pearson correlation coefficient r_{p} between the epoch-averaged fields of two layers—photosphere (ph), lower chromosphere (cL) and middle chromosphere (cM)—with the two-tailed probability p. Columns 7–9 list the epoch-averaged longitudinal magnetic fields themselves, in gauss, for the photosphere (mean $\langle B_{\mathrm{p}} \rangle$), the lower chromosphere (mean $\langle B_{\mathrm{cL}} \rangle$) and the middle chromosphere (mean $\langle B_{\mathrm{cM}} \rangle$), respectively. Within each stellar block an “Overall” line combines all epochs of that star and gives the correlation coefficients and mean fields derived from the full decade-long data set.

StartDate	EndDate	ObsCount	rp(ph,cL)	rp(ph,cM)	rp(cL,cM)	mean($\langle B_{\mathrm{p}} \rangle$)	mean($\langle B_{\mathrm{cL}} \rangle$)	mean($\langle B_{\mathrm{cM}} \rangle$)
AD Leo								
2006-1-11	2006-6-12	7	(0.33,0.46)	(0.25,0.59)	(0.42,0.35)	-284	-87	127
2007-1-27	2007-6-25	9	(-0.14,0.71)	(-0.13,0.74)	(0.62,0.08)	-275	-129	70
2008-1-19	2008-2-16	14	(-0.22,0.45)	(-0.57,0.03)	(0.83,0.00)	-254	-78	137
2011-12-1	2012-1-16	10	(-0.40,0.26)	(-0.69,0.03)	(0.74,0.02)	-231	-114	101
2016-2-17	2016-4-20	10	(0.27,0.46)	(0.49,0.15)	(0.52,0.12)	-187	-34	129
2019-11-15	2019-11-21	6	(0.61,0.20)	(0.47,0.34)	(0.73,0.10)	-190	-125	29
Overall	Overall	56	(0.26,0.05)	(-0.19,0.17)	(0.64,0.00)	-238	-91	106
YZ CMi								
2006-1-13	2006-2-7	2	-	-	-	0	-153	-100
2007-1-26	2007-2-8	7	(0.79,0.03)	(0.36,0.43)	(0.82,0.02)	-392	-295	-201
2007-12-28	2008-2-16	25	(0.84,0.00)	(0.65,0.00)	(0.79,0.00)	-358	-193	100
2009-1-30	2009-1-30	1	-	-	-	-204	-184	-1
Overall	Overall	35	(0.76,0.00)	(0.36,0.03)	(0.76,0.00)	-340	-211	26
EV Lac								
2005-7-17	2005-9-18	5	(0.59,0.29)	(0.60,0.28)	(0.84,0.07)	-54	-19	216
2006-8-5	2006-8-12	7	(0.98,0.00)	(-0.53,0.22)	(-0.50,0.26)	-161	-92	270
2007-7-28	2007-8-18	13	(0.84,0.00)	(-0.45,0.12)	(-0.57,0.04)	-83	-131	257
2009-6-4	2009-8-15	4	(0.75,0.25)	(-0.45,0.55)	(-0.92,0.08)	161	60	41
2012-8-14	2012-8-22	5	(0.97,0.01)	(0.00,1.00)	(0.18,0.77)	-1	-24	47
2016-7-15	2016-8-12	13	(-0.18,0.55)	(0.09,0.77)	(0.37,0.21)	-54	-126	88
Overall	Overall	47	(0.69,0.00)	(-0.35,0.02)	(-0.18,0.22)	-54	-84	167